Journal of the European Ceramic Society 43 (2023) 2958–2967

Contents lists available at ScienceDirect

Journal of the European Ceramic Society

journal homepage: www.elsevier.com/locate/jeurceramsoc

Matrix cracking onset stress and strain as a function of temperature, and characterisation of damage modes in SiC_f/SiC ceramic matrix composites via acoustic emission

Z. Quiney [a,*], S.P. Jeffs [a], L. Gale [b], S. Pattison [b], M.R. Bache [a]

[a] Institute of Structural Materials, Faculty of Science & Engineering, Swansea University, SA1 8EN, United Kingdom
[b] Rolls-Royce plc, P.O. Box 31, Derby DE24 8BJ, United Kingdom

ARTICLE INFO

Keywords:
Acoustic emission (AE)
Pattern recognition
Ceramic matrix composite (CMC)
Matrix cracking
Damage accumulation

ABSTRACT

The complex damage mechanisms that accumulate within SiC_f/SiC ceramic matrix composites (CMCs) subject to thermal and mechanical stress are being investigated in anticipation of the material's introduction into high performance gas turbine engines. Acoustic emission (AE) is recognised as a leading non-destructive evaluation (NDE) tool to this end, and was used in this study to determine the so-called matrix cracking onset stress under tensile load as a function of temperature up to a maximum of 1100 °C. Onset stress was interpreted using three traditional measurements based on AE energy characteristics during monotonic tests to failure. Pattern recognition (PR) analysis was performed on the AE data, revealing a specific cluster of signals that correlated closely with the initial matrix cracking region of the stress-strain curve. Taken in isolation, the onset stress of this activity was significantly lower than the conventional value. PR results were investigated further, and isolated clusters were linked to damage modes anticipated at other specific regions of the stress history. A secondary series of experiments was performed on specimens representing the individual constituents of the CMC (single-phase SiC flexural bars, Hi-Nicalon™ fibre bundles and SiC_f/SiC mini-composites) in attempts to further validate the corresponding AE signal characteristics. Matrix cracking and interphase debonding/sliding damage modes could be identified consistently, while fibre breaks remained difficult to isolate under the current experimental conditions.

1. Introduction

SiC_f/SiC Ceramic matrix composites (CMCs) are a key material in the design of next-generation gas turbine engines. Certain hot-section components such as blades and vanes, traditionally manufactured from nickel-based superalloys, are exposed to temperatures in excess of 1000 °C and require internal cooling systems accordingly. Due to superior thermal properties, CMCs could reduce or eliminate the requirement for such cooling systems, and combined with decreased density, improve the overall efficiency of engines. Superior oxidation/corrosion resistance offers a further advantage of the material.

A comprehensive understanding of the microscale and macroscale damage mechanisms and evolution under mechanical and thermal stresses is therefore sought. It is generally accepted that the initial phase of damage accumulation in these materials under uniaxial tensile mechanical stress is the initiation and propagation of micro-cracks in the matrix, which eventually form macro-scale through-thickness cracks. Cracks propagate between the matrix, interphase and fibres leading to debonding and interfacial sliding as the crack opening displacement and overall strain increases. Subsequently, the load is supported entirely by the fibres aligned with the direction of applied force, which fail progressively until the point of ultimate rupture [1]. Acoustic emission (AE) is ideally suited to a study of these mechanisms as each produces elastic stress waves that, in theory, should result in distinct corresponding waveform signatures.

AE analysis of CMCs can take various forms. Traditionally, AE energy (a measure of the area formed beneath the envelope of a discrete AE event waveform, $x(t)$) is the key parameter that provides a general indication of damage within a specimen under common loading regimes such as monotonic or unload-reload tensile [2,3], cyclic fatigue [4,5,6] and flexural [7] testing. A cumulative AE energy curve is often the chosen method of data visualisation. Through correlation with the

* Corresponding author.
E-mail address: z.a.quiney@swansea.ac.uk (Z. Quiney).

https://doi.org/10.1016/j.jeurceramsoc.2022.10.042
Received 24 June 2022; Accepted 15 October 2022
Available online 21 October 2022

anticipated strain regions of SiC_f/SiC CMC damage modes [8], the energy of individual 'soft' and 'loud' events has been linked to micro and macro matrix cracking at lower strains, and fibre failures and interlaminar cracking at higher strains [9]. The overall energy trend also indicated the assumed point of matrix crack saturation.

The AE onset stress (σ_{onset}) and strain (ε_{onset}) in SiC_f/SiC CMCs can be defined via extrapolation of the approximately linear portion of the normalised cumulative AE energy vs stress (and strain) curve to the zero-crossing value [10]. This definition of σ_{onset} has been shown to correspond well with both proportional limit and onset of fibre-bridged matrix cracks in various SiC/SiC CMCs, and can be considered equivalent to the matrix cracking stress [11,12]. Furthermore, it has been shown that cumulative energy has a close relationship with the measured 2-dimensional matrix crack density [10]. Our own research has made efforts to demonstrate the same relationship in 3-dimensional volumetric damage measurements [13]. σ_{onset} can also be defined by the applied stress at which the first 'loud' event is detected – where 'loud' is defined as having an energy (or sometimes amplitude) value within the highest order of magnitude of all gauge events [3]. Additonally, Morscher and Pjuar [11] demonstrate via a rule of mixtures relationship that σ_{onset} values are lower and more narrowly distributed for a range of SiC/SiC CMC materials when only the stress in the "minimatrix" (all material outside of the region formed by load-carrying 0 ° fibres, their CVI interphase and CVI SiC layer) is considered.

Pattern recognition tools have become increasingly popular during the last 30 years as a means of characterising AE signals in relation to specific damage modes. Ono [14] reviewed several such approaches as early as 1994, and more recent advances have been summarised by Muir et al. [15]. This approach can be highly successful when applied to polymer matrix composites [16,17,18], as the dissimilar mechanical properties of the materials comprising the matrix and reinforcement phases naturally give rise to distinct waveforms. CMCs, however, are not as straightforward as the material phases generally have similar properties. Nevertheless, previous researchers have been able to achieve this to some extent in differing CMC materials. Moevus et al. [19] used the unsupervised *k*-means clustering approach to characterise damage modes in two different types of SiC/[Si-B-C] composites under tensile load. The key modes that could be separated were associated with different forms of matrix cracking, interface crack propagation and interfacial debonding, but it remained difficult to isolate fibre failures from the full dataset. It was noted that a larger number of output clusters may lead to one damage mode being separated into multiple clusters, and that multiple damage modes were still present in a single cluster. Momon et al. [20] took the same initial approach and subsequently used the output clusters as training data to inform a supervised *k*-nearest neighbours classifier (*k*-NNC) algorithm. This improved the accuracy of the identification of damage modes including individual and multiple fibre failures, matrix cracking, debonding, sliding and crack closure in C/SiC CMCs tested between 700 and 1200 °C.

This study investigates the AE onset stress between room temperature (RT) and 1100 °C of a SiC_f/SiC CMC in air using three traditional measurement techniques. Cluster analysis was then performed using an unsupervised k-means algorithm in order to assess the importance of particular signals that were detected in advance of σ_{onset}, whilst also evaluating the general ability to characterise the various AE release mechanisms throughout the test to failure. A secondary series of experiments was performed in an attempt to validate the association of AE signal clusters with particular damage modes. The specimens involved in these secondary experiments included flexural bars of single-phase SiC, SiC_f/SiC CMC mini-composites and Hi-Nicalon™ fibre tows.

2. Materials and methods

2.1. Materials

The SiC_f/SiC CMC material was manufactured in the form of square plates consisting of 16-ply 0–90° 2D woven Hi-Nicalon™ fibre reinforcement, boron nitride interphase and matrix phase formed via a combination of chemical vapour infiltration (CVI) and melt infiltration (MI). Some additional detail of the manufacturing process has been discussed previously [21]. For the primary $\sigma,\varepsilon_{onset}$ test matrix, dog bone specimens were extracted from these CMC plates so that the nominal gauge section measurement was 40 mm in length, 10 mm in width and 4.7 mm (as manufactured) in thickness.

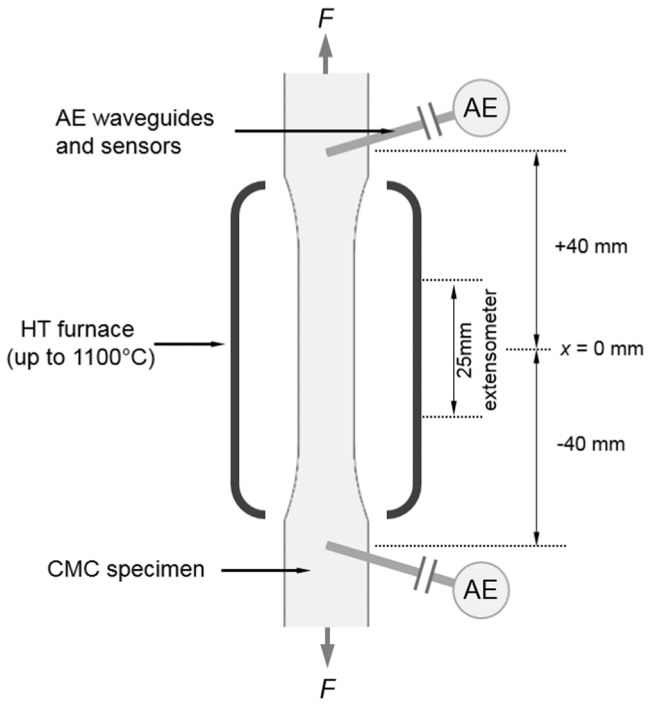

Fig. 1. High temperature $\sigma,\varepsilon_{onset}$ test configuration.

A secondary series of AE signal validation experiments was performed on alternative specimen types. Single-phase "matrix" specimens were in the form of reaction bonded SiC (RBSC) rectangular bars, with nominal dimensions 3 × 4 × 44 mm. Fibre bundle specimens were cut from Hi-Nicalon™ fibre tow containing nominally 500 fibres, a figure quoted by the supplier but not measured. Mini-composite specimens consisted of a single uniaxial fibre bundle of Hi-Nicalon™ fibres, coated with nominally 0.5 μm of BN interphase, and surrounded in CVI SiC matrix. Volume fractions were measured by the manufacturer as 26.8%, 3.2% and 70.0% respectively.

2.2. Experimental methods

2.2.1. Primary $\sigma,\varepsilon_{onset}$ Tests

Testing was performed on a Zwick Roell servo-hydraulic universal testing machine fitted with water-cooled hydraulic wedge grips. A schematic test diagram is provided in Fig. 1. Specimens were tested to failure under uniaxial monotonic tensile conditions, using displacement control at a rate of 0.5 mm/min. A two-zone high-temperature split furnace was used to heat the gauge length of the specimens. Temperature was monitored with two type-N thermocouples in contact with specimen gauge section in each zone within the furnace. Upon stabilisation of the required specimen temperature, a 30-minute soak period was employed prior to the start of the test. Any temperature variation was within 1% of the specified test temperature. Strain was measured via a 25 mm extensometer with ± 2 mm range.

2.2.2. Secondary AE validation tests

All AE validation testing was performed at RT on a Zwick Roell Z5.0 tensile frame with 5000 N load capacity.

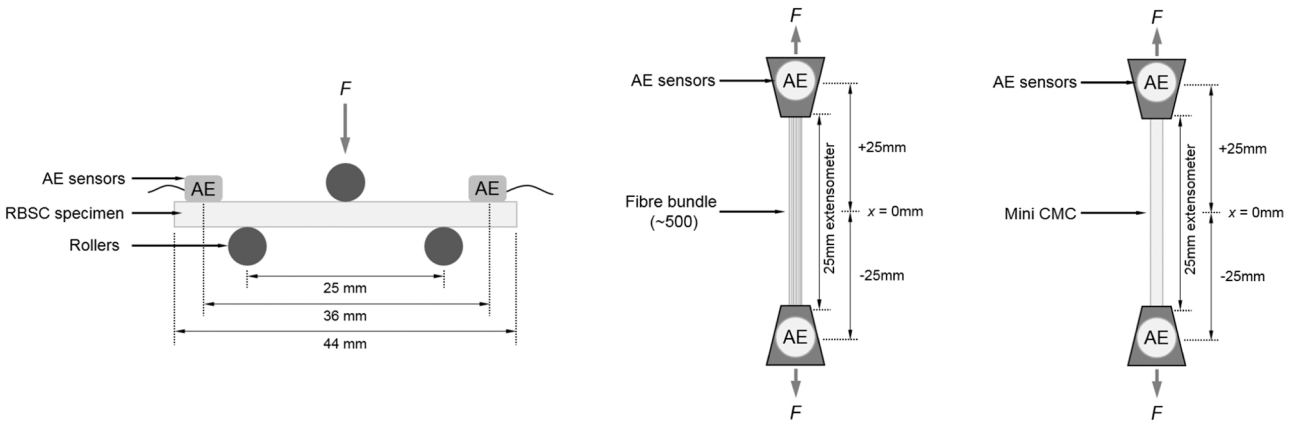

Fig. 2. Validation experiment test configurations.

RBSC flexural bars were tested in a three-point bend configuration. A 10 N preload was applied to the specimen prior to a displacement-controlled ramp at a rate of 0.1 mm/min until failure. A linear variable displacement transducer (LVDT) was used to acquire deflection measurements from the centre point of the lower surface.

Hi-Nicalon™ fibre bundles and mini-composite specimens were cut into sections of approximately 70 mm. These were bonded between steel tabs using an epoxy adhesive in a bespoke jig to ensure that alignment and gauge length was consistent. A gauge length of 22 mm remained exposed, chosen so that strain could be measured by a traditional 25 mm extensometer with the arms contacting the tabs. This approach was taken to reduce the risk of the extensometer applying undesired lateral forces to the specimen under direct contact. Once bonded, the specimen assembly was transferred into bespoke form grips fitted to the test machine. A preload of 10 N was applied to ensure the specimen was fully seated and aligned, before being tested under monotonic tensile conditions at a displacement-controlled rate of 0.2 mm/min.

2.3. AE system

AE was sampled at 5 MHz using a Mistras/Physical Acoustics Micro-II Express 2-channel AE system. Data acquisition and live displays were managed with the AEWin software package, and all post-processing was performed within the Mistras NOESIS software package. In all experiments a sensor pair was used in combination with a time-of-flight algorithm that rejected AE events not originating within the gauge section (or region of interest) of the specimens. Wideband AE sensors were selected as their broad frequency response range provided a greater depth of analysis possibilities than resonant sensors, which tend to have their frequency domain dominated by the resonant peak.

2.3.1. Primary $\sigma,\varepsilon_{onset}$ tests

The PAC WD sensor pair used in these experiments have a frequency range of 100–1000 kHz with a cylindrical footprint of Ø18 mm. Due to high temperatures these were mounted on stainless steel waveguides with a conical concentrator, approximately 120 mm in length. Contact with the specimen was maintained by spring force from bespoke rapid-prototyped clamps fitted to the upper and lower hydraulic wedge grip housing. The waveguides contacted the specimen at the upper and lower extremes of the furnace housing, with a waveguide tip offset of 80 mm. In this configuration the sensors remained close to ambient temperature (up to a furnace temperature of 1100 °C). The attenuation effect of the waveguides on AE signals was measured at around 30–32 dB (amplitude). Signals were amplified using a PAC 2/4/6 switchable preamplifier set at 60 dB, where typically 20 or 40 dB would be selected for an equivalent test at room temperature with sensors mounted directly onto the specimen surface. For consistency, waveguides were used at all temperatures including RT.

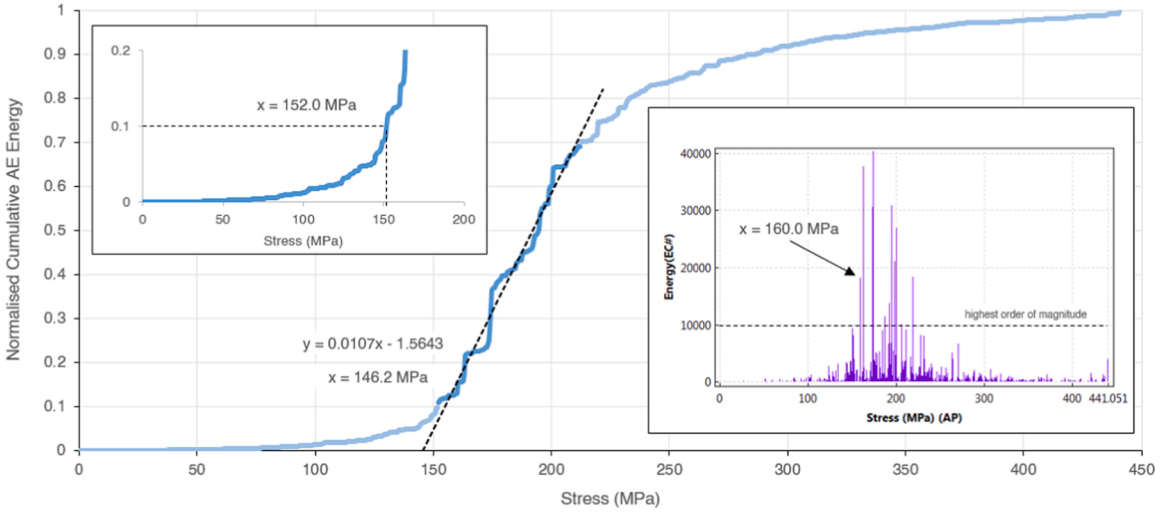

Fig. 3. Methods of measurement of σ_{onset} from AE data, including the linear intercept of normalised cumulative AE energy versus stress (primary plot), 10% of total cumulative AE energy (inset top-left), and first 'loud' event (inset bottom-right). The same techniques are applicable for ε_{onset} when the axes are plotted with respect to strain.

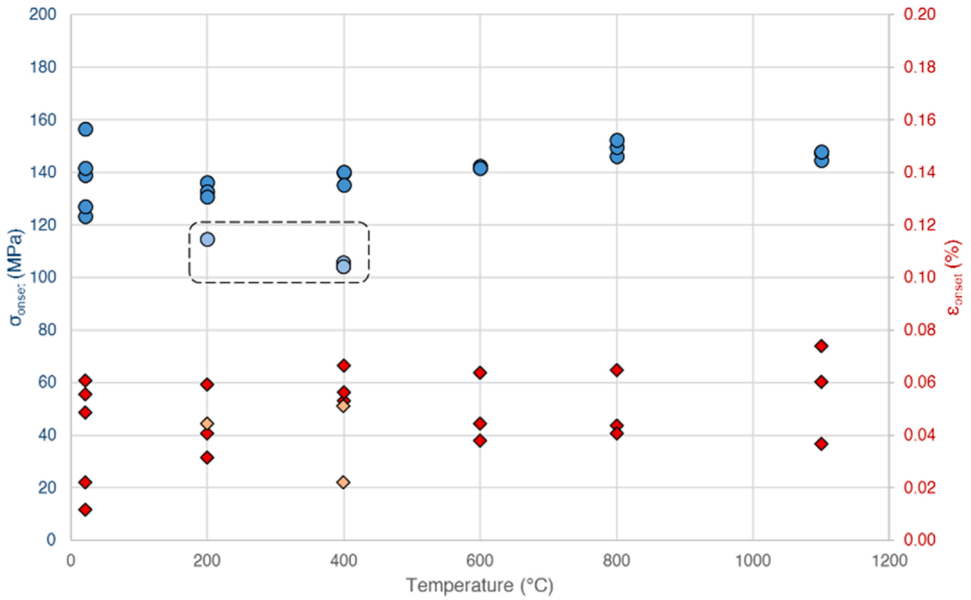

Fig. 4. Distribution of σ_{onset} and ε_{onset} as a function of temperature utilising the linear intercept measure. Three outlying stress results are circled, attributed to material variability. Their equivalent ε_{onset} values are denoted by the pale red markers, noting that low onset stress does not necessarily correspond to low onset strain in these cases.

2.3.2. Secondary AE validation tests

For these experiments, a much smaller PAC HD2WD sensor pair was used. These had a frequency range of 150 to 1850 kHz and a footprint of approximately 4 × 8 mm. Sensors were mounted either on the outer surface of the tabs (mini-composite and fibre bundle tests) or directly on the specimen upper surface (RBSC tests). While not detailed here, several back-to-back tests were performed to confirm that the two different sensor types (WD and HD2WD) produced a similar response to the AE under investigation. All specimen details and test conditions were summarised in 2.1 and 2.2.2; schematic test diagrams are shown in Fig. 2. Mechanical test data was recorded but is not relevant to the scope of this AE-driven study.

3. Results

3.1. σ,ε_{onset} test results

Parametric load and extension measurements from the test rig were converted to stress and strain values and imported into the NOESIS AE post-processing software where plots of cumulative AE energy vs stress and strain were generated. This data was subsequently exported to allow for precise analysis of σ_{onset} and ε_{onset}, which were measured in three different ways:

i. the $y = 0$ intercept of the trendline through the linear portion of the normalised cumulative AE energy vs stress (strain) curve [10] (herein referred to as the "linear intercept" measurement),

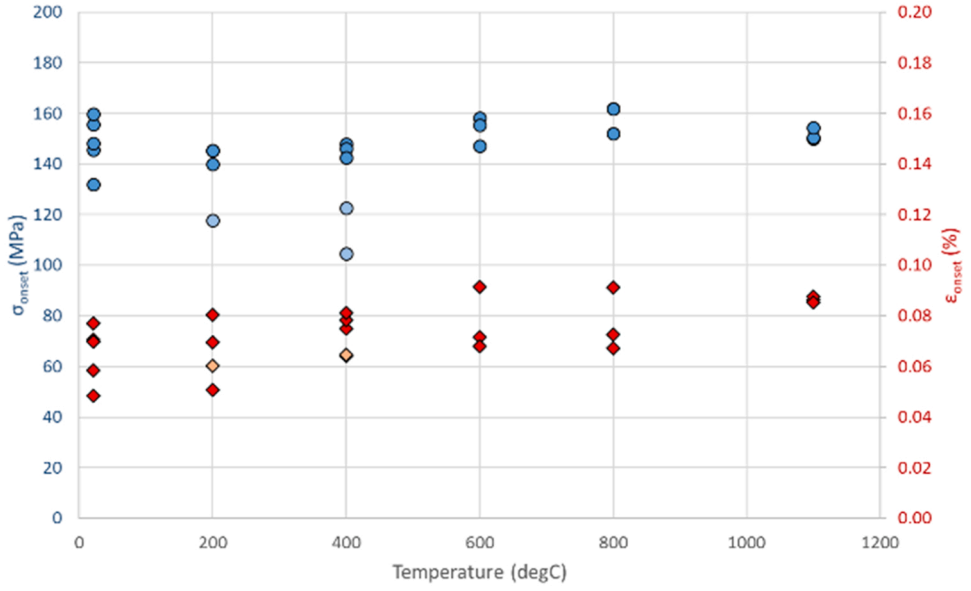

Fig. 5. Distribution of σ_{onset} and ε_{onset} as a function of temperature utilising the 10% total energy measure. The results are similar to the linear intercept measure, and again indicate the same three outlying stress results (pale-coloured markers).

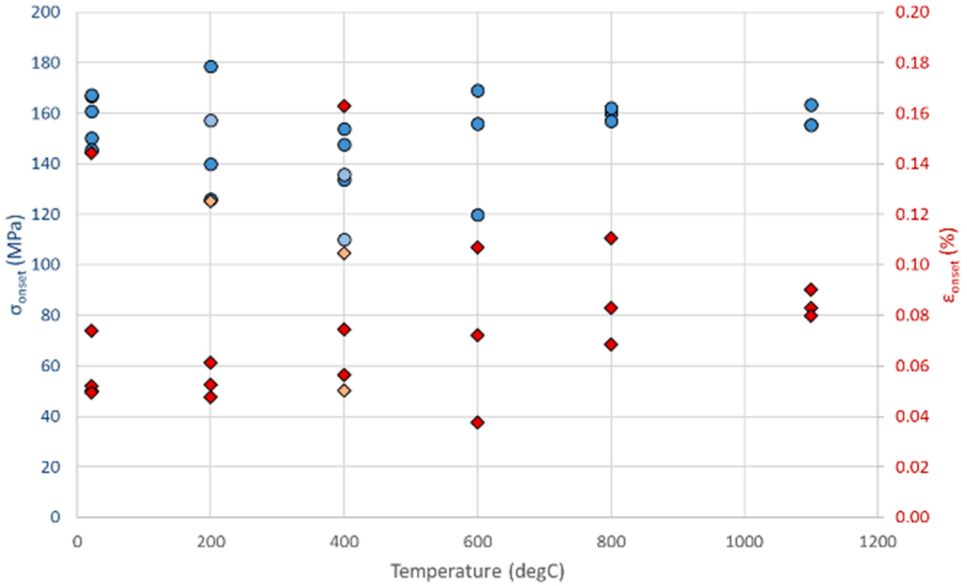

Fig. 6. Distribution of σ_{onset} and ε_{onset} as a function of temperature utilising the first 'loud' event measure. The degree of scatter in the data demonstrates the low reliability of this method. The three outlying stress results (pale-coloured markers) identified previously would not be noted by this measure.

ii. the stress (strain) at which the first AE event with an energy value in the highest order of magnitude is recorded [3] (herein referred to as the "first loud event" measurement),
iii. the stress (strain) at which 0.1 of the normalised cumulative AE energy is reached, adapted from the normalised *n%* method [22] (herein referred to as "10% energy" measurement).

An initial test plan of three repeats at each temperature was expanded to address higher scatter in the RT results and inconsistent onset stress at 200 °C and 400 °C (Fig. 4). The additional test results fell back in line with the overall averages, i.e. no further unusually low onset stresses were encountered. The anomalies were attributed to material/specimen variability. However, it should be noted that each of the specimens with a low AE onset stress measured a typical UTS value.

Discounting the three low-stress anomalies, the linear intercept (Fig. 4) and 10% energy (Fig. 5) measurements returned a relatively consistent set of σ_{onset} and ε_{onset} values. While there exists a notable drop in UTS between 800 °C and 1100 °C, there appeared to be little change in σ_{onset} across all temperatures. It is possible to interpret a small increasing trend in σ_{onset} and ε_{onset} up to 800 °C using both measurement methods, but all values expect one fell within the scatter of the RT tests (approximately 120–160 MPa). The numerical values are in line with published data for similar materials [3,10,11].

The first loud event measure produced a greater scatter in the data and the highest overall estimate of σ_{onset} and ε_{onset} (Fig. 6). Measuring a single datapoint rather than a trend rendered the method more susceptible to inconsistency and there was potential to overlook significant events falling just below the boundary of an order of magnitude (e.g. Fig. 3). This was reflected in the standard deviation of σ_{onset} and ε_{onset}, which is greater in the case of the first loud event (16.4 MPa and 0.032% respectively) than the linear intercept (13.5 MPa and 0.015%) and 10% energy (14.0 MPa and 0.012%) measurements.

According to Guillaumat and Lamon [8], damage accumulation in the region $\varepsilon = 0.025$–0.12% in a woven Nicalon, C interphase, CVI SiC CMC is associated with the earliest microcracking damage that initiates from pores between fibre plies. ε_{onset} is observed in the region of $\varepsilon = 0.01$–0.08% (Fig. 4), providing good evidence that these initial AE signals can be confidently associated with this mode of damage. What is more, this AE was detectable even with the use of waveguides.

3.2. Unsupervised pattern recognition results

3.2.1. Data pre-processing

AE signals comprise a variety of measurable waveform features that can be used to classify their difference or similarity to each other. Features were selected based on complete link hierarchical clustering, plotted via dendrogram representation, with only features below the normalised distance (similarity) threshold of 0.9 being chosen for further consideration. The 12 features selected for further processing were risetime, counts to peak, energy, duration, amplitude, average signal level, average frequency, root mean square, reverberation frequency, initial frequency, frequency centroid and peak frequency. Features with a normalised distance value close to 1 indicated that little to no further meaningful separation existed in the data, and these were not considered. Due to different units and scales of measurement for the selected features, all values were normalised in the range [− 1:1]/maximum standard deviation.

A principal component analysis (PCA) can be used at this stage to reduce the dimensionality of the data to be processed. Fundamentally, the principal components (PCs) are eigenvectors of the correlation matrix of the twelve-feature dataset that represent the most significant variances [19,23]. The number of PCs to be used for clustering can then often be reduced to a smaller number that still account for the majority of variance in the data. In the current study, the number of PCs, *j*, was chosen so that the degree-of-fit accounted for at least 95% of the variance in the original data (based on correlation matrix rather than covariance analysis). In practice, *j* was equal to 8 or 9 for the selected tests to be analysed. It is worth noting that in the reported datasets there was no appreciable difference in the final clustering results or computational processing time if PCA was not applied to the twelve selected features.

3.2.2. k-means clustering

At this stage it is necessary to highlight that there was an expectation that the waveguides might cause enough signal distortion that the PR analysis would be negatively impacted [24]. Thus, a small number of additional RT tests were performed with AE sensors coupled directly to the CMC specimen surface to act as a reference. Preamplifier gain was reduced to 20 dB accordingly. All other test conditions were identical to those reported in 2.2.1. These additional tests were not included in the AE onset analysis reported in 3.1.

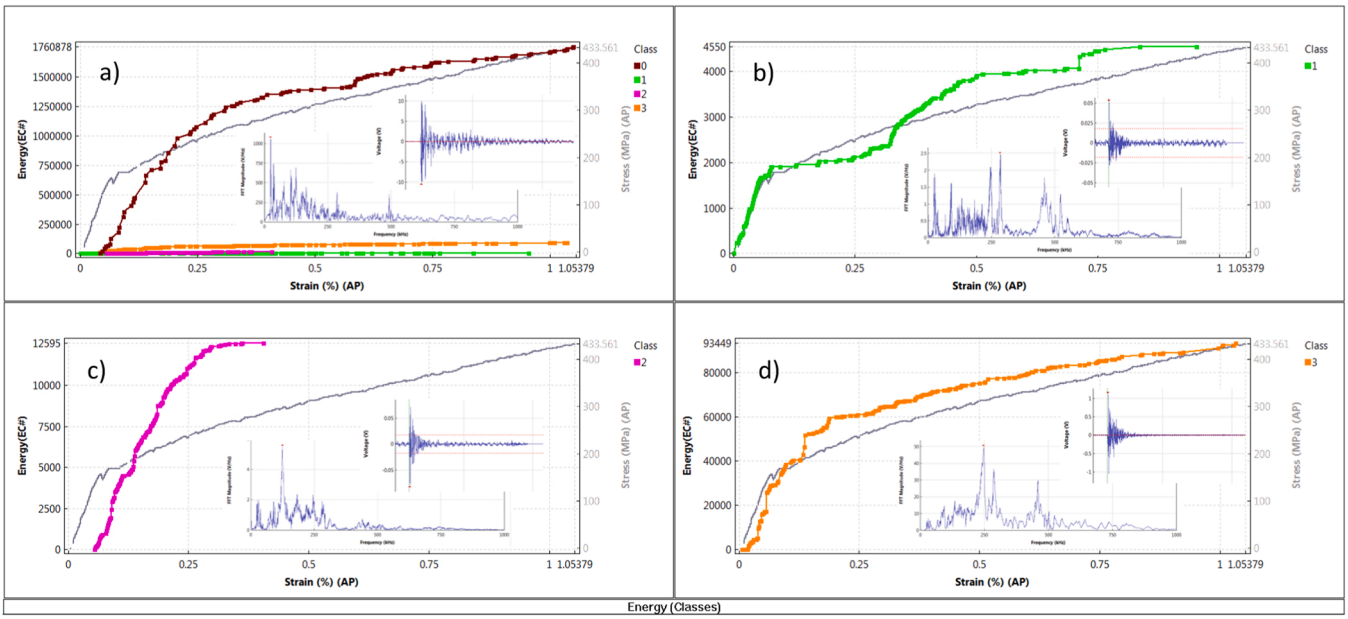

Fig. 7. Cumulative AE energy of four clusters of signals identified during a RT monotonic test to failure. AE sensors were coupled directly to the specimen. a) All clusters, indicating the large difference in energy of Cluster A(0), b) Cluster B(1), c) Cluster C(2), d) Cluster D(3). Inset: typical time-domain waveform and frequency spectrum (0–1000 kHz) from each cluster A-D respectively. The stress versus strain curve is superimposed in the background.

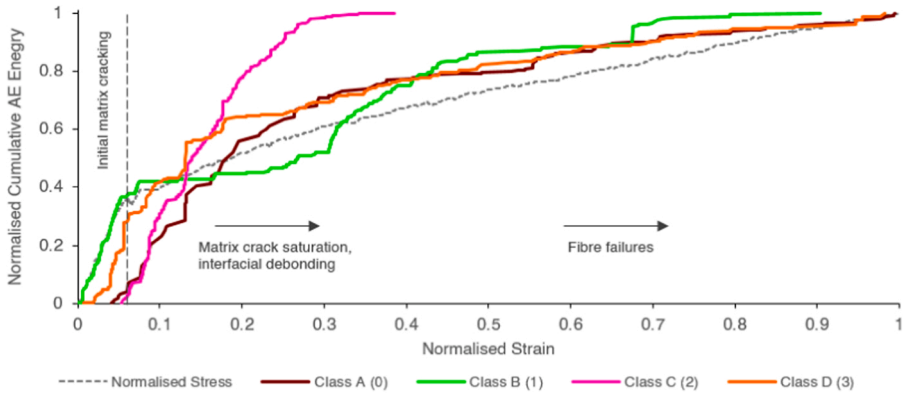

Fig. 8. Normalised cumulative AE energy of Clusters A-D identified in Fig. 7, demonstrating that different types of signal are active during different regions of expected damage with respect to the stress versus strain curve.

In the absence of a defined set of training signals that can be used to inform a supervised PR algorithm, unsupervised clustering must be used to extract information on the separation of datapoints. The *k*-means algorithm is ideally suited to AE signal analysis of composites as the primary input is the number of clusters, *k*, to be returned. In an ideal scenario one could assume this is equal to the number of different AE release mechanisms described by the signals in the data. For CMCs these would typically be matrix cracking, interfacial cracking/debonding, frictional sliding/pullout and fibre breakage (possibly expanded to include sub-categories of these primary modes). Naturally, it was anticipated that the investigation would not be so perfectly realised in practice, but this provided the basis for a short optimisation study with values of *k* between 3 and 6. For tests in which sensors were coupled to the specimen surface, the optimal result was found with $k = 4$. Where waveguides were used, the optimal result was found with $k = 5$.

Operation of the *k*-means algorithm begins with the selection of *k* initial points/centroids from the dataset, which in this study were chosen through random initial partitioning. All other data points are then assigned to their nearest centroid, measured here via Euclidean distance. The centroid is then re-positioned at the mean average of all points in that cluster, and the process is repeated until convergence or a defined number of iterations is reached, in this case 100. The algorithm was run multiple times to ensure the results were consistent. Occasionally, one or two clusters differed after 100 iterations, in which case the algorithm was repeated until it was clear that one result occurred more frequently than the other, and the common result was saved. The location filter was activated so that all AE datapoints had been measured as originating within the 40 mm gauge length of the specimen. The results were plotted as cumulative AE energy per cluster, superimposed with the stress versus strain curve for each specimen. A typical clustering result from one such test is given in Fig. 7, and is discussed in terms of the four clusters identified. Each cluster was then normalised, and plotted on a single graph to further highlight the regions of activity of each signal type with respect to the stress versus strain curve (Fig. 8).

Cluster A(0): contains mainly high-energy AE events, indicating that the energy feature still accounts for the greatest degree of variability in the data after normalisation. The cumulative energy of this cluster follows the same trend as the total (non-clustered) cumulative energy.

Cluster B(1): contains events of the lowest energy and amplitude. It is active immediately as the stress increases until the end of the

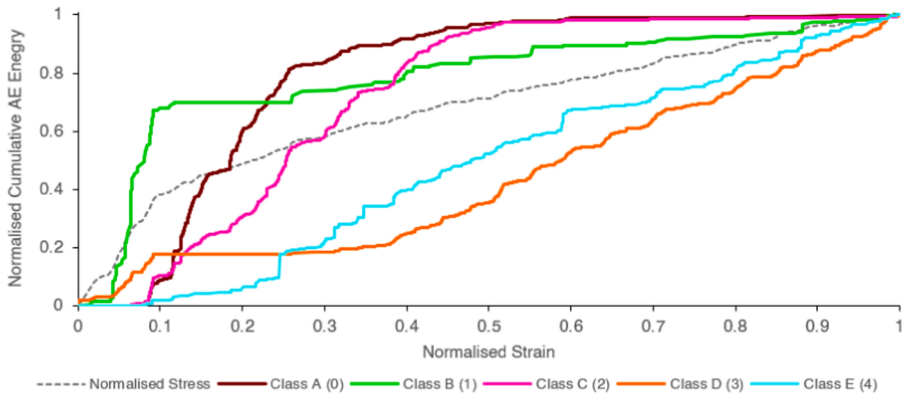

Fig. 9. Normalised cumulative AE energy of five clusters of signals identified during an 800 °C monotonic test to failure. AE was detected via waveguides, which may have somewhat impacted the classification ability of the algorithm. Nevertheless, similar clusters to Fig. 8 could still be identified.

proportional region of the stress vs. strain curve. This is highly indicative of a correlation with matrix micro-cracking and crack saturation. Similar signals have previously been associated with matrix cracking in CMCs by other researchers [19]. Beyond approx. 0.25% strain this cluster begins to accumulate again, suggesting that another mechanism with similar waveform properties is responsible. At this stage of the stress vs. strain curve this activity is more likely to be associated with interfacial debonding or sliding/pullout.

Cluster C(2): contains slightly higher energy events than cluster B, and becomes active near the end of the proportional region of the stress vs. strain curve. Furthermore, this cluster ceases activity before the second phase of accumulation in cluster B. These signals are therefore assumed to correspond to interfacial sliding or interfacial cracking/debonding.

Cluster D(3): is active throughout the test, including the initial proportional region. The energies of events are typically higher energy than cluster B, which suggests some degree of correlation with larger matrix crack behaviour. Beyond the proportional region, events in this cluster were partially defined by having lower average frequency than clusters A-C. It was difficult to associate this cluster with one specific mechanism.

The analysis was repeated on datasets where signals were acquired through waveguides. In most cases, such as the example in Fig. 9, equivalent clusters A, B and C could all be identified. Optimum classification was achieved with $k = 5$, resulting in two additional clusters. In terms of energy levels and initial accumulation, Cluster D was somewhat similar to that of Fig. 8, and also shared aspects of Cluster B, i.e. a secondary phase of accumulation possibly linked to a different mechanism at higher strain. One could suggest a correlation with fibre breakage, although given that fibre breaks did not appear to be separated in tests with no waveguides, this seems unlikely. It is assumed that the activity of Cluster D here is more a result of indistinct, homogenised AE signals due to waveguide distortions rather than specific material behaviour at higher temperatures. A fifth Cluster E contained extremely low energy signals that were consistent throughout the duration and not revealing of any particular mechanism. Increasing values of k could not separate these clusters with any greater clarity.

Cluster B is assumed to represent matrix microcracking due to its relationship with the stress vs. strain curve and waveform signal properties such as low amplitude, low energy and short duration observed in other research [19]. It is therefore notable that these signals are active well in advance of the previously calculated σ_{onset} of 152 MPa (Fig. 4). Taken in isolation, the linear intercept σ_{onset} for the matrix cracking activity (cluster B) in Fig. 9 was just 58 MPa. This may be related to the

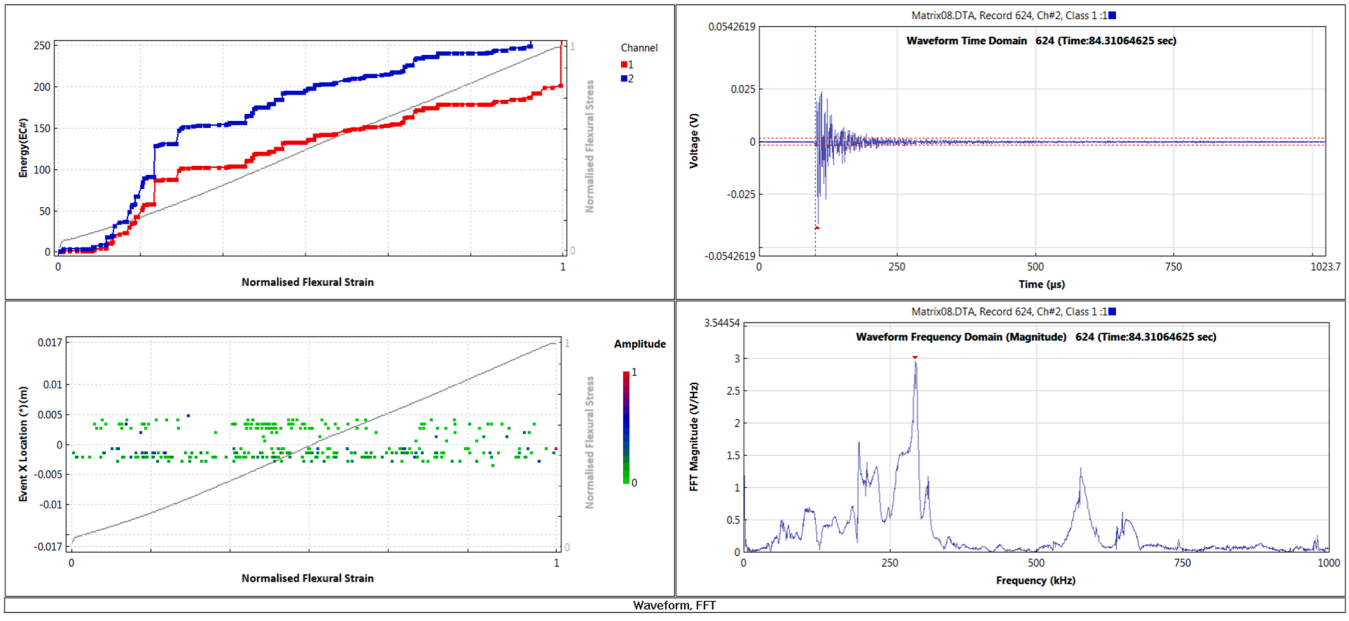

Fig. 10. Typical AE analysis of RBSC test. Top-left: cumulative AE energy on channels 1 and 2, bottom-left: linear location of AE events, top-right: typical time-domain waveform of a signal associated with cracking damage, bottom-right: FFT of the same signal.

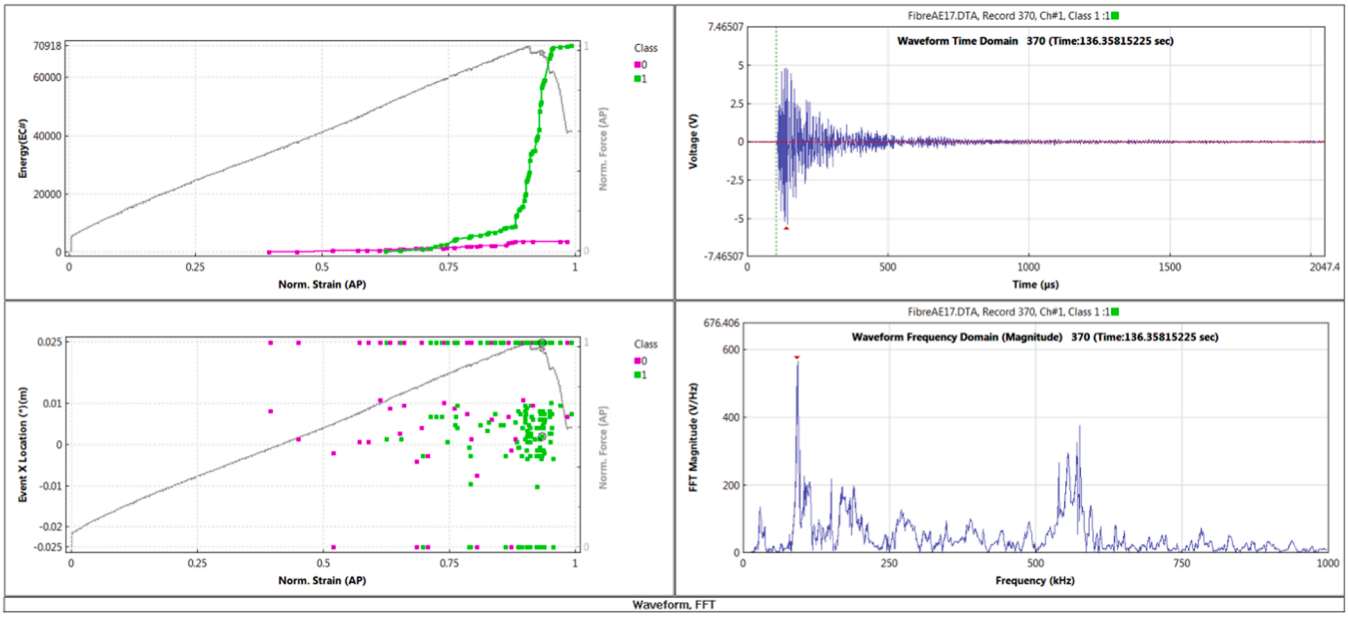

Fig. 11. Typical AE analysis of fibre bundle test. Top-left: cumulative AE energy of two identified clusters that were assumed to correspond with frictional interactions of fibres (class 0) and fibre breaks (class 1), bottom-left: linear location of AE events, top-right: typical time-domain waveform of a signal associated with a fibre break, bottom-right: FFT of the same signal.

"minimatrix" damage (onset stress ~ 95 MPa) discussed by Morscher and Pujar [11]. Energies and amplitudes may provide a justification to disregard this activity as insignificant, however there is demonstrably a degree of irreversible damage accumulating even at these low stresses.

A drawback of the PR analysis applied to the CMC material is that fibre breakage signals could not be conclusively separated. This may be because the signal properties are too similar to a different AE release mechanism, or because the position of the AE sensor surface (perpendicular to the load-carrying fibre orientation) is not conducive to elastic wave transmission.

3.3. Validation experiments

To further verify that the clustered AE signals do correspond to the assumed mechanisms, and additionally to try and identify fibre breakage signals, a series of validation experiments was carried out. First, pure RBSC flexural bars, representative of the matrix phase of the CMC, were tested in a three-point bend configuration in attempts to reproduce matrix crack-like AE signals. Secondly, as-manufactured Hi-Nicalon™ fibre bundles were tested to failure under monotonic tension to produce fibre break signals. Finally, SiC_f/SiC mini-composite specimens were tested to failure under monotonic tension to assess the resultant AE on a more controlled, localised scale.

3.3.1. RBSC specimens

All fractures occurred in the centre of the RBSC beam specimens. A location filter was used to ensure that the analysed AE occurred in this region. AE was detected throughout the test, although the 'largest' events occurred at around 25–50% of ultimate flexural stress. Overall, the measured amplitudes and energies of all events were very small and displayed a very short risetime. Peak frequencies were in the region of 250–300 kHz, with additional notable frequency components in the region of 600 kHz (Fig. 10). These characteristics were entirely consistent with the matrix cracking signals from the CMC material specimens.

3.3.2. Fibre specimens

A location filter was used to ensure that the analysed AE occurred between the metallic tabs onto which the specimen was bonded. The total number of AE hits sometimes exceeded the number of fibres in the tow (500, as quoted by the supplier), thus it was assumed that some AE arose from frictional interactions of the fibres as well as fibre breaks. A simple k-means cluster analysis was performed on this data using $k = 2$,

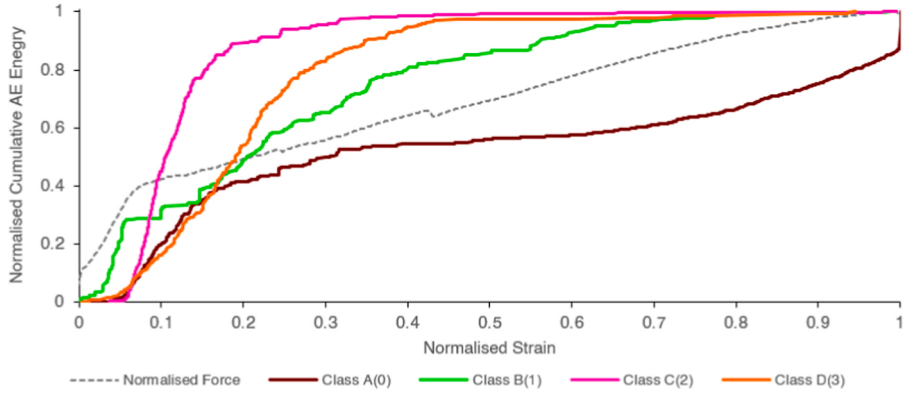

Fig. 12. Normalised cumulative AE energy of four clusters of signals identified during a mini-composite monotonic test to failure. The clusters show some resemblance to those identified for CMC dog bone specimens.

Table 1
Correlation of assumed damage modes and AE signal characteristics in all specimen types investigated.

Assumed Damage Mode (s)	AE Signal Characteristics	Found in Specimen Type
SiC matrix cracking/ microcracking	• Very low amplitude • Very low energy • Frequency components at ~100–300 kHz and ~500–600 kHz	• SiC_f/SiC CMC dog bone • Single-phase RBSC flex bar • SiC_f/SiC mini-composite
Larger cracking events	• Medium to high amplitude • Frequency components at ~250 kHz and ~500 kHz • Higher frequency centroid • Occurs to some extent in proportional stress/strain region • Mostly occurs before 0.5 normalised strain	• SiC_f/SiC CMC dog bone • SiC_f/SiC mini-composite
Interfacial cracking/ debonding, sliding	• Low to medium amplitude • Low to medium energy • Low peak frequencies and low frequency centroid • Initiates immediately after proportional limit	• SiC_f/SiC CMC dog bone • SiC_f/SiC mini-composite
Currently not associated (generic 'high energy' cluster)	• Very high amplitude • Very high energy • Long decay • Low frequency centroid • Present throughout test but mostly after proportional limit	SiC_f/SiC CMC dog bone
Fibre failures	• Medium to high amplitude • Medium to high energy • Frequency components at ~100–250 kHz and ~600 kHz • Slightly longer risetime than matrix cracking signals	Hi-Nicalon™ fibre bundle

which found two clusters separated predominantly by relatively high and low energies. The high energy cluster occurred at the approach of peak load and was more comparable to the total number of fibres (accepting that multiple fibres must fail simultaneously and therefore it is impossible for the DAQ timing parameters to distinguish each individually). Thus, events from this cluster were inspected to gain an understanding of fibre break signal characteristics. Signal waveforms had considerably higher amplitude and energy than matrix cracking signals, and a longer risetime than all other classes of signal investigated in this study. Peak frequency was generally in the region of 100 kHz, although strong frequency components existed at 600 kHz also (Fig. 11). These characteristics are reasonably consistent with those of fibre breaks in a C/SiC composite [20].

3.3.3. SiC_f/SiC mini-composite specimens

A location filter was applied in the same way as the fibre bundle specimens. The cumulative AE energy followed a very similar trend to the CMC dog bone specimens investigated in this study, with an additional increase in the gradient as the specimen approached peak stress and strain. *k*-means cluster analysis was applied using $k = 4$, on the assumption that equivalent AE release mechanisms existed in both the CMC dog bone and mini-composite specimens. This was supported by the results shown in Fig. 12. Clusters A and B are fairly consistent with their counterparts in Fig. 8 and Fig. 9. Cluster D is less consistent, but in the context of the mini-composite test is most likely to correspond with frictional sliding of the fibres and interphase due to the cluster's low energy and because it reaches higher strains than cluster C, which is assumed to correspond to interfacial cracking/debonding. The composition of the uniaxial mini-composite, and particularly the variability of the surrounding matrix layer, possibly explains why matrix cracking (cluster B) does not accumulate and saturate in quite the same manner in as in woven laminate dog bone specimens. Cluster A is most likely to contain fibre break signals, although if true these are mixed with more general high energy events throughout the test. Studying the waveforms, all mini-composite waveform characteristics were approximately consistent with the signals analysed in 3.2.2, 3.3.1 and 3.3.2.

A summary of waveform characteristics from all tests is provided in Table 1.

4. Conclusions

Three methods of determining AE-based σ_{onset} and ε_{onset} in SiC_f/SiC CMC dog bone specimens under monotonic tensile stress at elevated temperatures up to 1100 °C were investigated. The "linear intercept" and "10% total energy" metrics yielded reasonably consistent results, indicating a slight increase in σ_{onset} between RT and 800 °C and subsequent decrease in σ_{onset} at 1100 °C, and a slight increase in ε_{onset} between RT and 1100 °C. Using the "first loud event" resulted in a higher standard deviation and unclear trend in the σ_{onset} and ε_{onset} data.

There is good evidence that unsupervised pattern recognition (in the form of *k*-means clustering) can be used to classify matrix cracking, interfacial debonding/cracking and interfacial sliding AE release mechanisms. Further SEM or high-resolution XCT inspections would be required to prove this conclusively. The AE linked to matrix cracking initiated at significantly lower stresses than the traditional onset stress indicated by the full cumulative AE energy curve. Higher temperatures required the use of AE waveguides which caused some degree of signal distortion, although the same clusters of activity could still be detected with reasonable consistency. Fibre failures remain difficult to identify under the current conditions, potentially because their waveform signal properties are similar to other damage modes, or because the position of the AE sensor/waveguide is not conducive to elastic wave transmission. A series of validation experiments provided good evidence that signals associated with specific damage modes are consistent across different specimen types.

The energy feature of AE signal waveforms appears to be responsible for the greatest variation in the clustering results. Analysis might be improved with alternative algorithms or greater emphasis on other features such as frequency components. It is our intention to increase the frequency range of our AE investigations to 2 MHz in future. The experiments reported here provide a robust set of training data that may now be used in supervised pattern recognition approaches.

Declaration of Competing Interest

The authors declare that they have no known competing financial interests or personal relationships that could have appeared to influence the work reported in this paper.

Acknowledgements

This work was supported through funding from Innovate UK as part of CEMTEC (UKRI project reference 113160). The provision of materials and technical support from Rolls-Royce plc is also gratefully acknowledged.

References

[1] A. Kelly, Concise Encyclopedia of Composite Materials, Elsevier, 2012.
[2] G.N. Morscher, M. Singh, J.D. Kiser, M. Freedman, R. Bhatt, Modeling stress-dependent matrix cracking and stress–strain behavior in 2D woven SiC fiber reinforced CVI SiC composites, Compos. Sci. Technol. vol. 67 (6) (2007) 1009–1017.
[3] G.N. Morscher, N.A. Gordon, Acoustic emission and electrical resistance in SiC-based laminate ceramic composites tested under tensile loading, J. Eur. Ceram. Soc. vol. 37 (2017) 3861–3872.
[4] M. Moevus, D. Rouby, N. Godin, M. R'Mili, P. Reynaud, G. Fantozzi, G. Farizy, Analysis of damage mechanisms and associated acoustic emission in two SiC/

[Si–B–C] composites exhibiting different tensile behaviours. Part I: damage patterns and acoustic emission activity, Compos. Sci. Technol. vol. 68 (2008) 1250–1257.
[5] E. Maillet, N. Godin, M. R'Mili, P. Reynaud, J. Lamon, G. Fantozzi, Analysis of Acoustic Emission energy release during static fatigue tests at intermediate temperatures on Ceramic Matrix Composites: towards rupture time prediction, Compos. Sci. Technol. vol. 72 (2012) 1001–1007.
[6] M.R. Bache, C.D. Newton, J.P. Jones, S. Pattison, L. Gale, P.I. Nicholson, E. Weston, Advances in damage monitoring techniques for the detection of failure in SiCf/SiC ceramic matrix composites, Ceramics vol. 2 (2) (2019) 347–371.
[7] G. Ojard, D. Goberman, J. Holowczak, Acoustic emission as a screening tool for ceramic matrix composites, AIP Conf. Proc. 1806 (2017), 020027.
[8] L. Guillaumat, J. Lamon, Multi-fissuration de composites SiC/SiC, Rev. Des. Compsoites Et. Des. Mater. Av. vol. 3 (1993) 159–171.
[9] G.N. Morscher, Modal acoustic emission of damage accumulation in a woven SiC/SiC composite, Compos. Sci. Technol. vol. 59 (1999) 687–697.
[10] G.N. Morscher, Stress-dependent matrix cracking in 2D woven SiC-fiber reinforced melt-infiltrated SiC matrix composites, Compos. Sci. Technol. vol. 64 (2004) 1311–1319.
[11] G.N. Morscher, V.V. Pujar, Design guidelines for in-plane mechanical properties of SiC fiber-reinforced melt-infiltrated SiC composites, Int. J. Appl. Ceram. Technol. vol. 6 (2) (2009) 151–163.
[12] M.P. Appleby, D. Zhu, G.N. Morscher, Mechanical properties and real-time damage evaluations of environmental barrier coated SiC/SiC CMCs subjected to tensile loading under thermal gradients, Surf. Coat. Technol. vol. 284 (2015) 318–326.
[13] Z. Quiney, E. Weston, P.I. Nicholson, S. Pattison, M.R. Bache, Volumetric assessment of fatigue damage in a SiCf/SiC ceramic matrix composite via in situ X-ray computed tomography, J. Eur. Ceram. Soc. vol. 40 (2020) 3788–3794.
[14] K. Ono and Q. Huang, Pattern recognition analysis of acoustic emission signals, in The 12th International Acoustic Emission Symposium, Sapporo, Japan, 1994.
[15] C. Muir, B. Swaminathan, A.S. Almansour, K. Sevener, C. Smith, M. Presby, J. D. Kiser, T.M. Pollock, S. Daly, Damage mechanism identification in composites via machine learning and acoustic emission, npj Comput. Mater. vol. 7 (2021) 95.
[16] R. Gutkin, C.J. Green, S. Vangrattanachai, S.T. Pinho, P. Robinson, P.T. Curtis, On acoustic emission for failure investigation in CFRP: Pattern recognition and peak frequency analyses, Mech. Syst. Signal Process. vol. 25 (2011) 1393–1407.
[17] L. Li, S.V. Lomov, X. Yan, V. Carvelli, Cluster analysis of acoustic emission signals for 2D and 3D woven glass/epoxy composites, Compos. Struct. vol. 116 (2014) 286–299.
[18] W. Zhou, W.-Z. Zhao, Y.-n Zhang, Z.-j Ding, Cluster analysis of acoustic emission signals and deformation measurement for delaminated glass fiber epoxy composites, Compos. Struct. vol. 195 (2018) 349–358.
[19] M. Moevus, D. Rouby, N. Godin, M. R'Mili, P. Reynaud, G. Fantozzi, G. Farizy, Analysis of damage mechanisms and associated acoustic emission in two SiCf/[Si–B–C] composites exhibiting different tensile behaviours. Part II: unsupervised acoustic emission data clustering, Compos. Sci. Technol. vol. 68 (2008) 1258–1265.
[20] S. Momon, N. Godin, P. Reynaud, M. R'Mili, G. Fantozzi, Unsupervised and supervised classification of AE data collected during fatigue test on CMC at high temperature, Compos.: Part A vol. 43 (2012) 254–260.
[21] L. Gale, S. Harris, S. Pattison, J. Baker, J. Fowler, Development and evaluation of sub-element testing of SiC/SiC ceramic matrix composites at elevated temperatures, J. Eur. Ceram. Soc. vol. 41 (2021) 3167–3176.
[22] A.R.A. Abraham, K.L. Johnson, C.T. Nichols, R.L. Saulsberry and J.M. Waller, Use of Statistical Analysis of Acoustic Emission Data on Carbon-Epoxy COPV Materials-of-Construction for Enhanced Felicity Ratio Onset Determination, NASA Johnson Space Center, Houston, TX, United States, 2012.
[23] I. Jolliffe, Principal Component Analysis, Springer Series in Statistics, Springer, New York, NY, 2002.
[24] N. Godin, P. Reynaud, G. Fantozzi, Challenges and limitations in the identification of acoustic emission signature of damage mechanisms in composites materials, Appl. Sci. vol. 8 (2018) 1267.